Contents lists available at SciVerse ScienceDirect

# Estuarine, Coastal and Shelf Science

journal homepage: www.elsevier.com/locate/ecss

# A numerical study on the role of wind forcing, bottom topography, and nonhydrostacy in coastal upwelling

Lide Jiang [a,b,*], Xiao-Hai Yan [a], Yu-Heng Tseng [c], Laurence C. Breaker [d]

[a] Center for Remote Sensing, College of Earth, Ocean, and Environment, University of Delaware, Newark, DE 19716, USA
[b] CIRA at Colorado State University, Fort Collins, CO, USA
[c] Department of Atmospheric Sciences, National Taiwan University, Taipei 106, Taiwan, ROC
[d] Moss Landing Marine Laboratories, Moss Landing, CA 95039, USA

## ARTICLE INFO

## ABSTRACT

The responses of coastal upwelling to different magnitudes of wind stress over a narrow and a wide shelf are studied using a 3-D primitive equation numerical model. The results show that the position of the upwelling front depends on both the strength and the duration of the wind forcing. The comparison between different shelf widths shows that wide shelf will limit the cold water intrusion, so that the corresponding decrease in sea surface temperature is less compared to narrow shelves. Besides, the difference between hydrostatic and nonhydrostatic model results shows that nonhydrostatic effects will enhance the growth of surface meandering, and can be more pronounced near steep fronts. Although difference does exist, our results show that the nonhydrostatic effects are very small at least in this idealized study case.

## 1. Introduction

### 1.1. Upwelling off eastern and western boundaries

Coastal upwelling, due to its ecological and economic significance, has been extensively studied, especially along the west coast of North America (hereafter referred to as 'the west coast'), where there have been many measurements of upwelling-related processes (e.g., Smith, 1968; Wooster, 1981; Ikeda and Emery, 1984; Mooers and Robinson, 1984; Halliwell et al., 1986; Huyer et al., 1987; Rosenfeld et al., 1994). Although less intense and less studied, upwelling off the east coast of North America (hereafter referred to as 'the east coast'), has been frequently observed and reported, e.g., along Florida's Atlantic coast (Taylor and Stewart, 1959; Pitts and Smith, 1997), off North Carolina (Wells and Gray, 1960; Knowles and Singer, 1977), in the Georgia Bight (McClain et al., 1984) and off New Jersey (Glenn et al., 1996; Yankovsky and Garvine, 1998; Clemente-Colon and Yan, 1999; Song et al., 2001). Compared to the west coast upwelling, where the major atmospheric circulation is favorable for upwelling over extended areas and time periods, east coast upwelling is more limited both temporally and spatially, because the local winds there

are often not strong enough to transport as much water into the surface layers (Smith, 1968) as along the west coast.

Although upwelling along the west coast and the east coast has long been studied, there has been inadequate focus on the comparisons between the two coasts. Smith (1968) has mentioned the existence of limited upwelling along the east coast, and attributed the less intensive upwelling along the east coast to the shorter duration of upwelling-favorable winds; Garvine (2004) has compared the inner shelf circulation off the New Jersey coast, with that of the west coast (Trowbridge and Lentz, 1991), and found that different ratios for the isopycnal slope to bottom slope are important factors affecting the local circulation.

It is well-accepted that different wind forcing and bottom topographies are two of the important factors that contribute to different upwelling intensities and scales along the two coasts. Wind drives the coastal upwelling process, while the bottom topographies are closely related to bottom boundary layer in which water flows onshore, driven by higher pressure offshore and bottom friction, to compensate for the offshore surface flow. In this study, we explore these differences of the two coasts using a numerical model, with simplified, idealized wind forcing and bottom topography, to gain some insights on the reasons for observed differences in both the intensities and spatial extents of west coastal and east coastal upwellings.

* Corresponding author. Present address: E/RA3, Room 102, 5200 Auth Road, Camp Springs, MD 20746, USA.
E-mail address: lide.jiang@colostate.edu (L. Jiang).

## 1.2. Numerical modeling of coastal upwelling

Numerical models specialized in coastal upwelling have evolved since the 1960's (O'Brien, 1967; O'Brien and Hurlburt, 1972). They have capabilities to address nonlinearity and the complex geometry/topography of the coast and shelf. The state-of the art in ocean modeling has progressed steadily over the past 30 years (e.g., Semtner, 1995; McWilliams, 1996). Ocean models are now fully 3-dimensional and based on the complete set of non-linear stratified primitive equations (e.g., Haidvogel and Beckmann, 1998). Representations of subgrid-scale mixing and diffusion effects have been improved significantly with the introduction of more realistic parameterizations (e.g., Pacanowski and Philander, 1981; Mellor and Yamada, 1982; Large et al., 1994). Vertical coordinate systems have become more flexible to better accommodate complex topography in the deep and coastal oceans (e.g., Bleck, 2002). More recently, unstructured-grid ocean models have been developed which can better fit the irregularity of coastal geometry, such as Delft3D (Ham et al., 2005), FEOM (Danilov et al., 2005), FVCOM (Chen et al., 2003), ICOM (Pain et al., 2005), and SLIM (Legrand et al., 2006; White and Deleersnijder, 2007). Finally, concurrent with more powerful computers, spatial resolution has increased greatly in recent years, and as a result, most models today are fully eddy resolving.

However, most of these models employ the hydrostatic approximation, which poses potential problems in modeling coastal upwelling, in which cases the Rossby radius is relatively small and nonhydrostatic effects can become significant (Tseng et al., 2005). The nonhydrostatic terms become important for features whose horizontal scale is not much larger than their vertical scale. In upwelling areas, the vertical acceleration may not be small compared to the buoyancy term; in such cases, there may be significant nonhydrostatic effects on horizontal velocity through vortex stretching, as well as on vertical velocities (Casulli and Stelling, 1998). Chao and Shaw (2002) used an idealized model to find that downward convection caused by unstable stratification in a nonhydrostatic model would hasten the growth of upwelling meanders and filaments. These meanders and filaments are surface manifestations of instabilities generated during upwelling, which have been frequently observed, e.g., in Bernstein et al. (1977), and reproduced in the laboratory (Narimousa and Maxworthy, 1985, 1987a,b, 1989). Tseng and Ferziger (2001) also showed that these instabilities can be better represented in a nonhydrostatic model.

The model used in this study is the Dietrich Center for Air-Sea Technology (DieCAST) ocean model (Dietrich, 1997; Tseng and Dietrich, 2004). It is a z-level, rectilinear coordinate model, which uses mixed Arakawa A and C grids, and a fourth-order interpolation scheme that provides high computational accuracy and low numerical dissipation (Dietrich et al., 2004). Z-coordinate models have an advantage over $\sigma$-coordinate models in that they are not prone to horizontal pressure gradient errors (Haney, 1991), while in $\sigma$-coordinate models the surfaces of constant $\sigma$ are not generally horizontal, especially over steep topography that is often found in areas of coastal upwelling (Beckmann and Haidvogel, 1993; Mellor et al., 1994, 1998). Tseng and Dietrich (2006) showed that z-coordinate models are robust with respect to model resolution and background viscosity, if higher-order advection schemes are used. They found that low dissipation can be used without sacrificing numerical stability and accuracy.

In this study, the hydrostatic and nonhydrostatic versions of the DieCAST model were used and compared. The nonhydrostatic version includes the acceleration term and the non-linear terms in the vertical momentum equation, which are omitted in the hydrostatic version. Tseng et al. (2005) used hydrostatic and nonhydrostatic versions of DieCAST to study the regional circulation in the Monterey Bay area. They found that nonhydrostatic effects were significant inside Monterey Canyon and near Pt. Sur, where the difference between hydrostatic and nonhydrostatic versions was mainly related to the coastal topography near the Sur Ridge.

In the following section, we describe the model setup. Model results are presented in Section 3, after which we present a discussion in Section 4 and a summary in Section 5.

## 2. Model setup

### 2.1. Model domain

The horizontal model domain is 100 km alongshore by 200 km cross-shore, with 1 km resolution in both directions. Periodic boundary conditions are applied along the two cross-shore boundaries. The alongshore domain size was chosen to be large enough to permit formation of features with length scale of less than 100 km, which is within major concern of the current study. The offshore boundary is closed at 200 km from the coast, where a sponge layer is imposed to dampen boundary effects. In this study, the area of concern is limited within 100 km from the coast, which is adequately far from the offshore boundary. 100 km is also large enough to cover the wide continental shelf for US east coast. Model depths range from 0 to 1000 m, and are divided into 20 levels, with level thickness increasing exponentially from 10 m near the surface to about 100 m near the bottom. The coordinates are defined as follows: $x$ is positive in the direction of Kelvin wave propagation, $y$ is positive offshore, and $z$ is positive upward. The model domain is in $f$-plane with $f = 10^{-4}$ s$^{-1}$.

### 2.2. Wind forcing

Upwelling-favorable wind stress is applied over the entire model domain according to: $\begin{cases} \tau_x = -\tau_0 \left[ 2 - e^{(y-200)/40} \right] \\ \tau_y = -\tau_0 e^{(y-200)/40} \end{cases}$, where $\tau_x$ and $\tau_y$ are the alongshore and cross-shore components of the wind stress, $y$ is the offshore distance in kilometers, and $\tau_0$ is specified different values in different simulations. Within 100 km from the coast, $(y = 0) \begin{cases} \tau_x \approx -1.99\tau_0 \\ \tau_y \approx -0.01\tau_0 \end{cases}$ and $(y = 100) \begin{cases} \tau_x \approx -1.92\tau_0 \\ \tau_y \approx -0.08\tau_0 \end{cases}$, the wind is primarily alongshore, and at offshore boundary, where $y = 200$, $\begin{cases} \tau_x = -\tau_0 \\ \tau_y = -\tau_0 \end{cases}$. The wind near the offshore boundary is purposefully deviated from the alongshore direction by 45° so that the local wind-driven surface current is nearly parallel to the boundary. The trick is done to reduce the influence of the solid wall at the offshore boundary. Although the wind stress is not strictly uniform in space, only about 7% of the spatial variation in wind stress is within 100 km of the coast. The wind stress curl induced Ekman pumping, which is calculated to be only about 0.14 m per day at 100 km offshore, is negligible within 100 km from coast.

A gradually ramped wind stress is applied to stationary ocean according to: $\tau(t) = \tau(1 - e^{-2t})$, where $t$ is the elapsed time in days. It increased from 0 to 86% of its limit in one day and is almost constant after two days. Four cases with different wind stresses are simulated, which we name W1, W2, W3 and W4, corresponding to $\tau_0 = 0.2$, 0.4, 0.6 and 0.8 dyn/cm$^2$, respectively. These values are chosen based on commonly observed values of wind stress (e.g., Nelson, 1977).

### 2.3. Bottom topography

Fig. 1 shows the vertical cross-sections for the two different bottom topography set-ups, one for the narrow shelf case (NR)
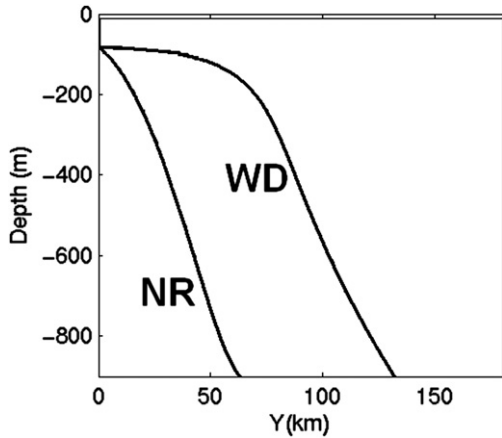
**Fig. 1.** Two bottom topography settings for the narrow (NR) and wide (WD) shelf.

similar to the US west coast, and the other for the wide shelf case (WD) similar to the US east coast. NR has a shelf width of about 10 km, and WD's shelf width is roughly 60 km. Different shelf widths result in different bottom slopes in near shore zone where coastal upwelling occurs. For the west coast, the bottom slope is approximately $9 \times 10^{-3}$, whereas for the east coast, it is approximately $1 \times 10^{-3}$, almost an order of magnitude smaller (Clarke and Brink, 1985; Lentz and Trowbridge, 1991; Garvine, 2004). In our model simulations, the bottom slope at NR's near shore zone is about $1/80 \sim O(9 \times 10^{-3})$, whereas at WD's near shore zone the bottom is almost flat.

### 2.4. Temperature

The initial temperature is specified over the entire model domain according to $T(z) = 5 + 10\exp(-0.25 \times 10^{-4} z^2)$, where $z$ is the depth in meters. The temperature is 15 °C at surface and asymptotically approaches 5 °C at depth. In this study, density is a linear function of temperature according to: $\sigma(z) = 2 \times 10^{-4}[12 - T(z)]$, where $\sigma$ is the density anomaly. The thermocline is centered at about 150 m depth, with the Brunt-Väisälä frequency maximum of $\sim O(0.01)\ \text{s}^{-1}$. A study of North Carolina inner shelf circulation by Lentz (2001) has shown that inner shelf circulation is strongly affected by stratification, and the inner shelf response to wind stress is very different under stratified than under unstratified conditions. Although in real situations temperature profiles off the west coast
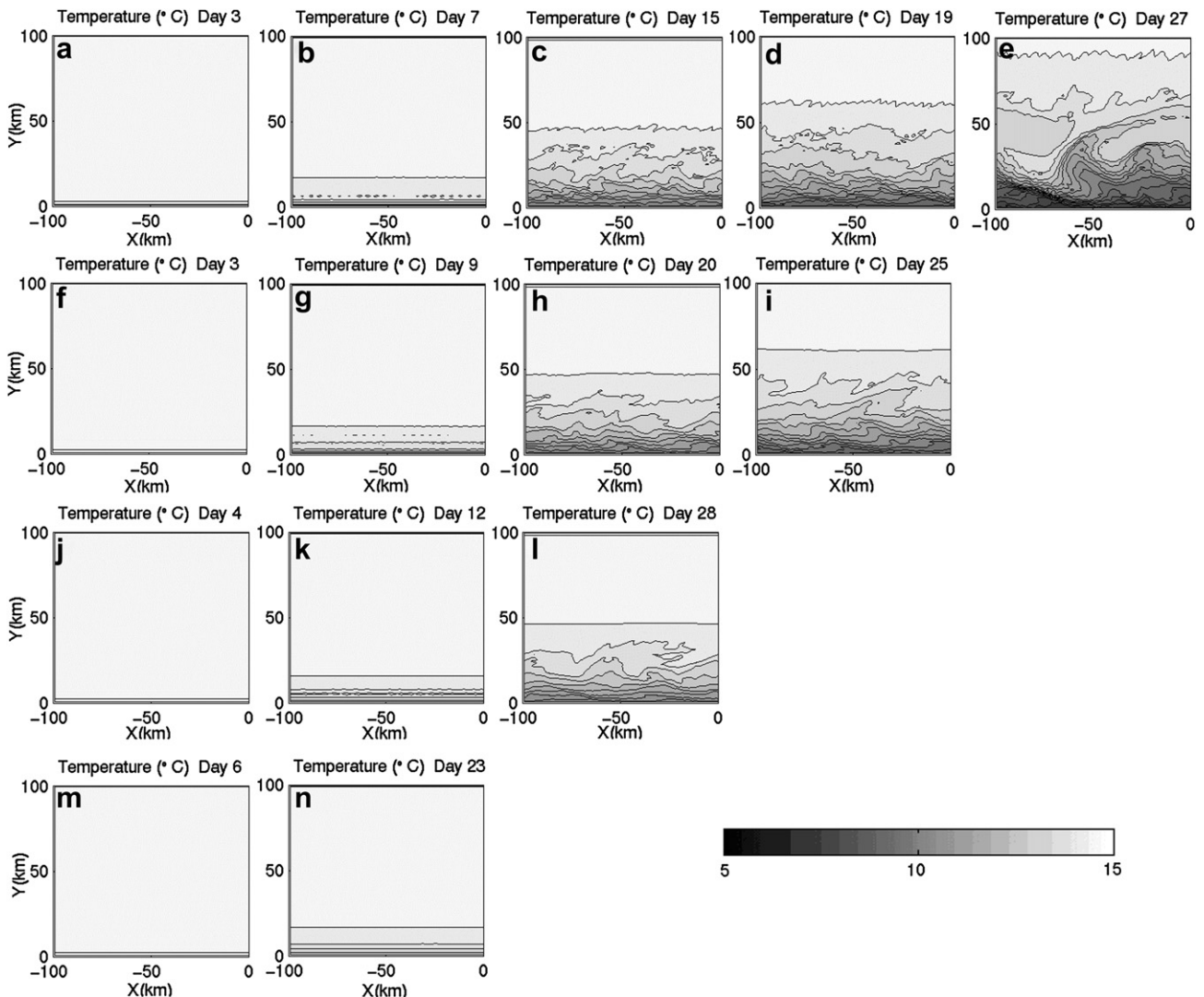


**Fig. 2.** Similar stages of surface temperature in the development of upwelling under wind stress of four different magnitudes (Fig. 2a–e: 1.6 dyn/cm²; Fig. 2f–i: 1.2 dyn/cm²; Fig. 2j–l: 0.8 dyn/cm²; Fig. 2m–n: 0.4 dyn/cm²).

and the east coast differ, we use the same the initial temperature profile for both topographies because the impact of stratification is out of the scope of this study.

## 2.5. Mixing scheme

For horizontal mixing the model uses a constant turbulent eddy viscosity and diffusivity, both of which are set equal to 5 m$^2$/s; while for vertical mixing, the scheme of Pacanowski and Philander (1981) is used. This turbulence closure scheme produces more realistic results than constant eddy viscosity profile (Pacanowski and Philander, 1981), while less sophisticated and computationally more efficient than the Mellor & Yamada 2.5 level turbulence closure model.

## 3. Model results

### 3.1. Experiment 1: different wind stress

This experiment is focused on the effect of wind stress on coastal upwelling circulation for the NR shelf topography. Fig. 2a–e shows the surface temperature evolution during the first 30 days under W4 wind forcing, corresponding to $2 \times 0.8 = 1.6$ dyn/cm$^2$ wind stress near the coast ($\sim 10$ m/s). At the end of day 3, cooler water starts to appear at the coast, indicating that the cooler water is caused by coastal upwelling instead of wind induced surface mixing, which would not have been limited to the coast. The thermal front appears as a straight line indicating uniform offshore transport. The front migrates steadily offshore, and by day 7, small features appear close to the coast, separated by about 4–5 km.

The features of the instabilities resemble those in Durski and Allen (2005), in which they are identified as baroclinic

instabilities fueled by the release of background potential energy due to the sloping isopycnal. These features later develop into wave-like motions. They first appear along the coast and gradually propagate offshore, producing small wiggles along the leading thermal front. With time, the leading thermal front continues to migrate further offshore and larger scale features start to appear near the coast. The scale of the cyclonic eddy forming by day 30 reaches $\sim 100$ km. Also by day 30, the leading thermal front has extended to 100 km offshore, and the surface temperature near the coast has decreased by more than 5 °C. Fig. 2e also shows a cold filament forming by day 27 (near $x = -50$ km, $y = 50$ km), a process often observed along the west coast during upwelling (e.g., Swenson et al., 1992). Note that the filament growth is restricted by the wall at 200 km offshore. However, if there were no such wall at the offshore boundary and the upwelling-favorable wind continued to blow, the filament would keep growing and eventually form a large eddy and propagate offshore (Allen et al., 1991). Such eddy shedding processes are frequently observed in California Current System. In a study by Haney et al. (2001), also using the DieCAST model to simulate the California Current System, they found the eddies propagate offshore to some point where they begin to redistribute their energy to deeper water through a process that converts baroclinic flow energy into barotropic flow energy.

The cross-section of the alongshore averaged temperature for NR-W4 is shown in Fig. 3a–c. The isotherms are tilted upward slightly, first in the bottom boundary layer, and then intersecting with the surface near the coast, forcing the warm surface water offshore. Because of the alongshore averaging, the instabilities are not visible. There is also weak downwelling at the offshore boundary, caused by the presence of the sponged wall. The existence of the wall has no significant impact on our results due to its distance, but it can limit the growth of filaments as we see in Fig. 2e.
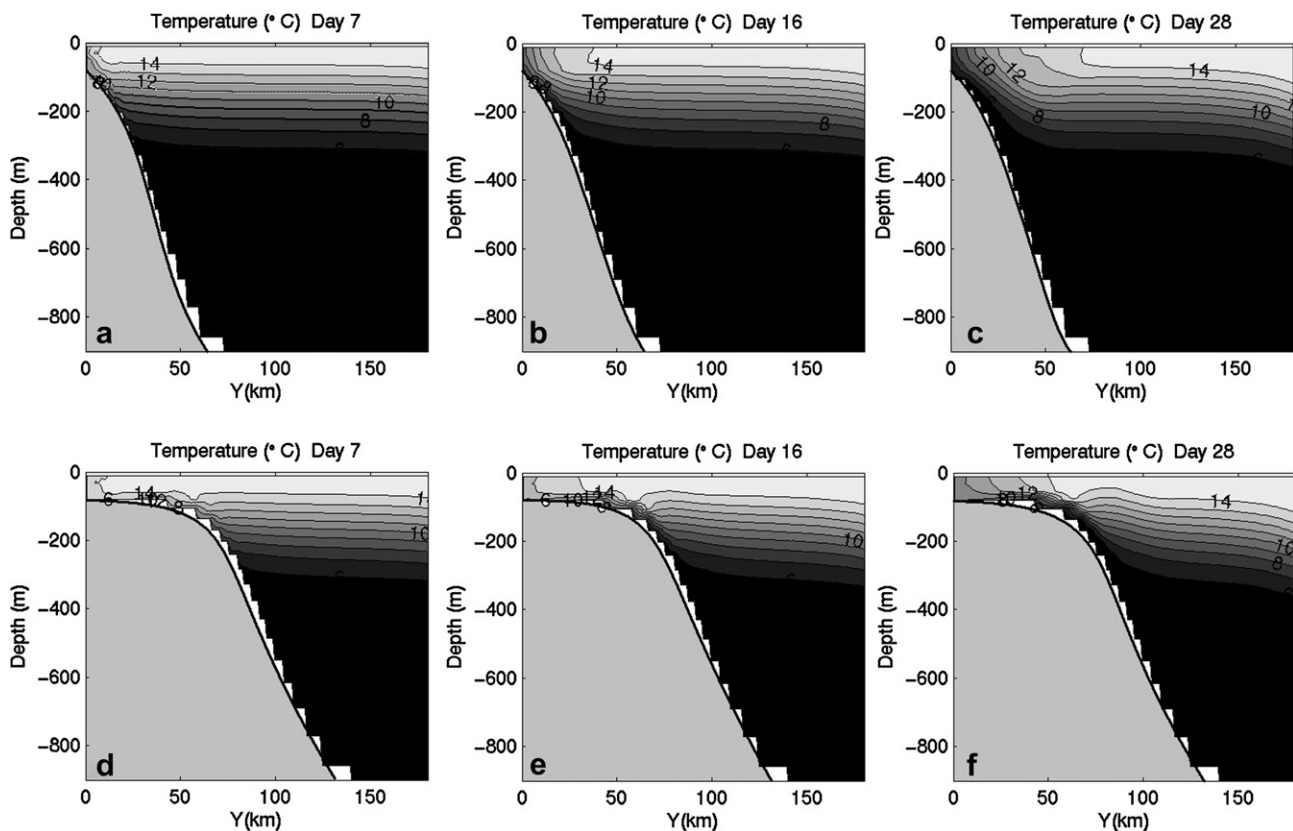


Fig. 3. Temperature cross-sections at progressing upwelling stages for: (a)–(c) the narrow shelf case (NR-W4); (d)–(f) the wide shelf case (WD-W4).
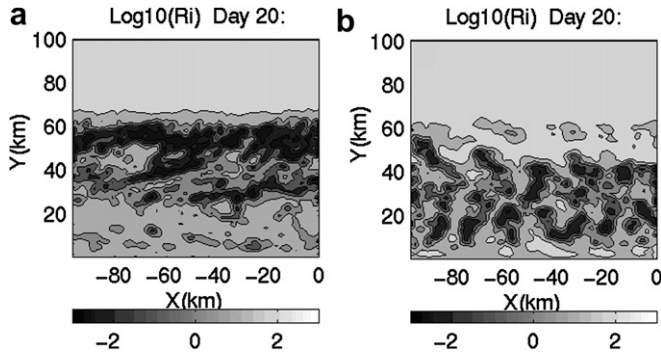
**Fig. 4.** Surface gradient Richardson number (in logarithm) at the end of day 20 for (a) NR-W4 (b) WD-W4.

We use W4 case as a reference for comparisons of different wind strength. Based on the location of the thermal fronts in Fig. 2a–e, we next select different wind strength W3, W2 and W1 to produce the results shown in Fig. 2f–i, j–l and m–n. For example, these figures show that instabilities start to emerge by day 7, 9, 12 and 23 for cases W4, W3, W2 and W1, respectively. The emergence of instabilities indicates that the extent of the isopycnal sloping is adequate to transform enough potential energy into eddy kinetic energy to produce instabilities that are visible in our model. From these results, we see that the development of coastal upwelling under different wind forcing is qualitatively similar, and that the time it takes to develop to a certain stage depends on the magnitude of the wind stress. The main difference is that stronger wind produces greater instability. In the strong wind cases, W4 and W3, there are always small wavy features along the leading thermal front, and for W4 they are more apparent than they are for W3. Conversely, there are no distinguishable features along the leading

thermal front in the weaker wind cases, W1 and W2. We also observe more smaller-scale features under strong wind conditions than under weak wind conditions.

Since our description of the model simulations of coastal upwelling are based mainly on the location of the thermal front, we proceed to define an upwelling front more rigorously. We use the gradient Richardson number for this purpose, since the upwelling front is characterized by strong mixing, in which case the local gradient Richardson number is often below the critical value of 0.25. The gradient Richardson number is defined as: $Ri = N^2/S^2$, where $N$ is the Brunt-Väisälä frequency and $S$ is the magnitude of vertical velocity shear: $S^2 = (\partial u/\partial z)^2 + (\partial v/\partial z)^2$.

Fig. 4a shows the gradient Richardson number near the surface at the end of day 20 for the NR-W4 run. White indicates gradient Richardson number $Ri > 100$ (or $\log_{10}(Ri) > 2$ as shown in the figure), which corresponds to very stable stratification; black indicates $Ri < 0.1$ (or $\log_{10}(Ri) < -1$), corresponding to well-mixed areas. Since the change of gradient Richardson number at the upwelling front is quite abrupt, we can easily use this boundary to identify the position of upwelling front. By visual inspection, for example, we notice that the upwelling front has propagated to about 65 km offshore by day 20.

Likewise, we can obtain the daily position of the upwelling front during the first 30 days for all four cases W1–W4. The results are summarized in Fig. 5. There are two phases in the upwelling front migration. In the first phase no instabilities appear, and the front migrates slowly, maintaining a straight line. The start of the second phase is defined by the appearance of a new front beyond the original front, seen by an abrupt increase in the offshore distance. In the second phase, the front migrates faster than in the first phase, and instabilities are apparent within the area of coastal upwelling. Offshore movement in the second phase is roughly 3.9, 2.8, 1.8 and 0.9 km/day (equivalent to 4.5, 3.3, 2.1 and 1.1 cm/s) for cases W4, W3, W2 and W1, respectively. Speeds during the first phase are
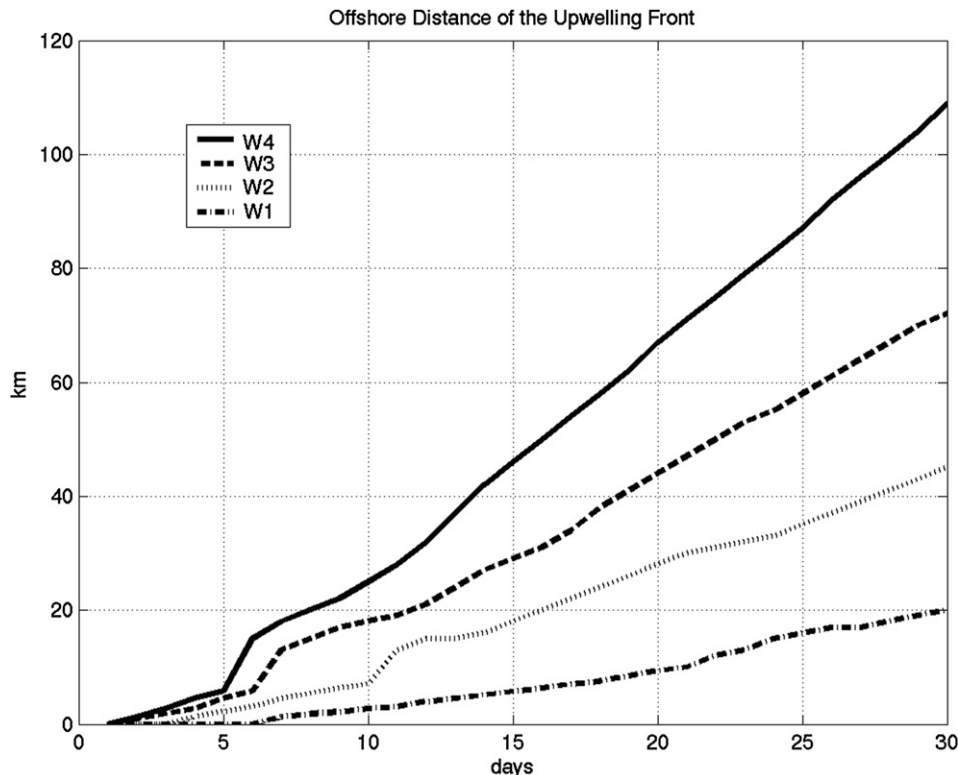


**Fig. 5.** Daily offshore positions of upwelling front, defined by the critical gradient Richardson number near the surface, under four different wind strengths.
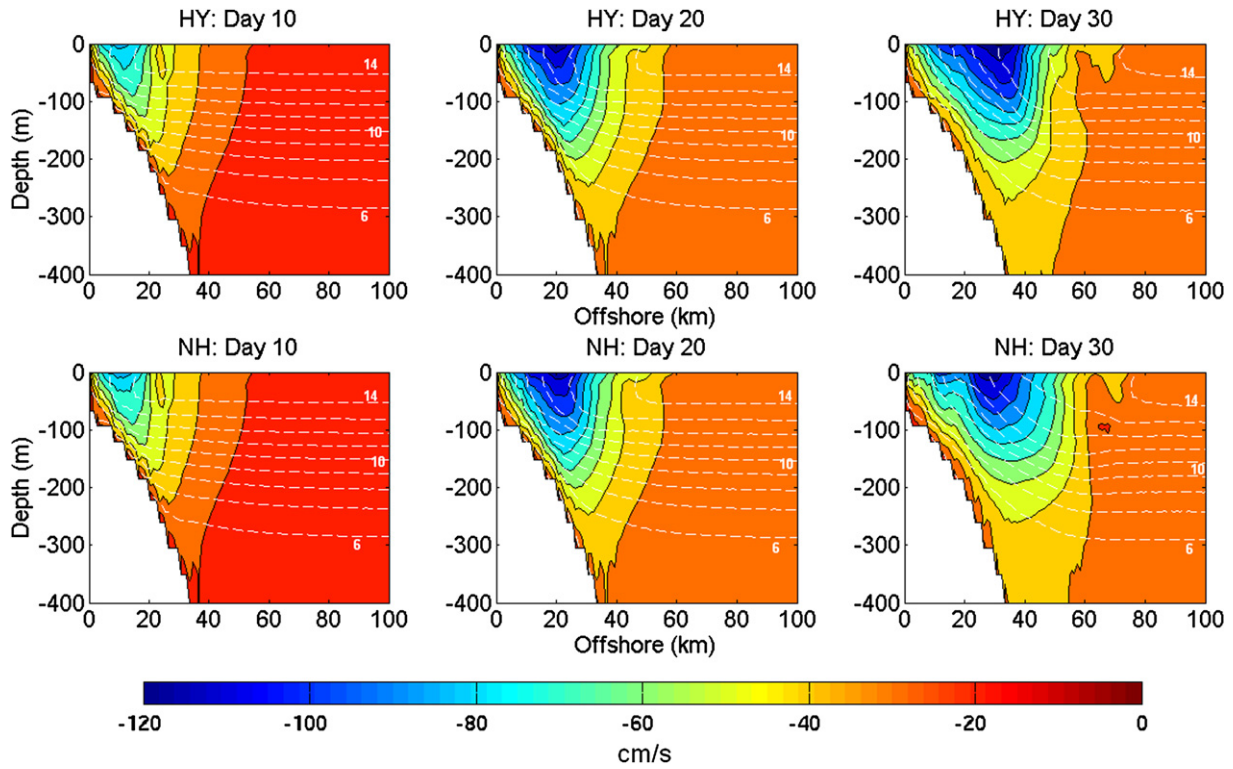
**Fig. 6.** Cross-section time sequences (NR-W4) from hydrostatic (HY) and nonhydrostatic (NH) model versions for alongshore velocity with temperature contours overlaid.
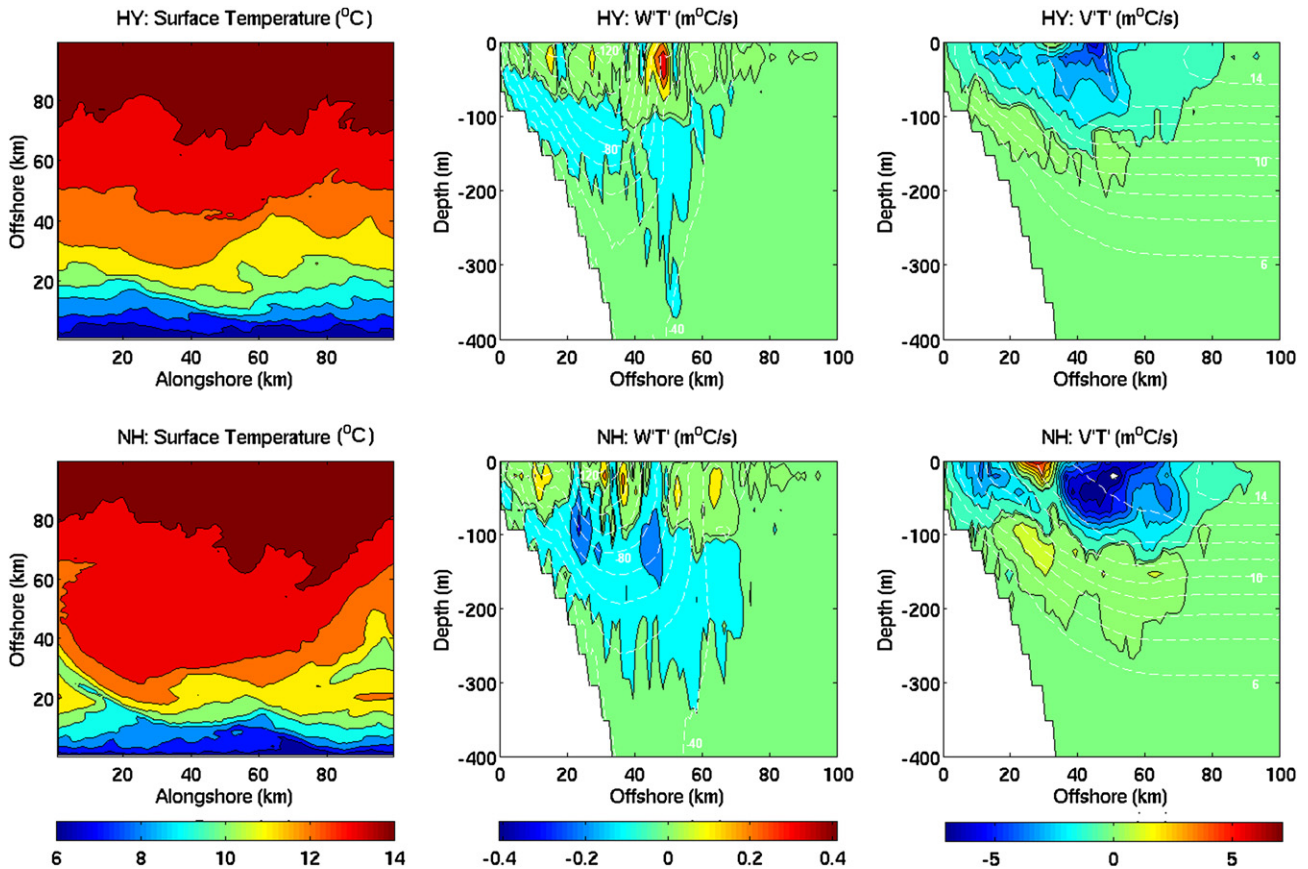


**Fig. 7.** The surface temperature, the alongshore-averaged w'T' overlaid with alongshore-averaged alongshore velocity, and alongshore-averaged v'T' overlaid with alongshore-averaged temperature, for HY(upper) and NH(lower) on day 30.

about 1.5, 1.2, 1.0 and 0.7 km/day, and the transitions occur on days 6, 7, 11 and 24.

## 3.2. Experiment 2: different shelf width

This experiment considers the effects of different shelf widths, a primary difference between the U.S. west and east coasts. A wide shelf translates into less cool source water, because deep water is available only further offshore compared to a narrow shelf. Also for the east coast inner shelves, the water depths are shallower and bottom friction becomes more important, and can induce more turbulent mixing.

The initial temperature profile we employ here is the same as for NR, and W4 winds are imposed (Fig. 3b). It is apparent in the figure that the wide, shallow shelf acts as a barrier for cold slope water to reach the inner shelf. However, as long as the wind forcing is maintained, cool water does appear on the inner shelf by day 7 (13−14 °C, close to the coast), but the temperature difference is smaller: 1−2 °C for WD compared to 3−4 °C for NR. Thus, when other conditions are comparable, wide shelves can limit the invasion of colder water, so that surface temperatures do not decrease as much. Displacement of the surface warm water by Ekman transport is also slightly less in this case compared to NR, which may be due to the slow-down effects of bottom friction on the shallow shelf for WD. The remarkably less temperature drop during upwelling for WD as compared to NR could partly explain the infrequent upwelling observed along the east coast: the surface temperature signature is not as obvious as along the west coast, even when wind is strongly upwelling-favorable. Of course, there are other factors that can contribute to the less-observed upwelling

along the east coast. For example, the warm Gulf Stream over the slope can make the upwelled water even less cool.

## 3.3. Experiment 3: hydrostatic vs. nonhydrostatic

In this experiment, two versions of the DieCAST model are used: hydrostatic and nonhydrostatic. Fig. 6a shows the vertical section of alongshore-averaged alongshore velocity with overlaid temperature from both the hydrostatic (HY, upper row) and nonhydrostatic (NH, lower row) model versions using NR-W4 case setup. Different columns show different days in the simulation. The alongshore velocity and temperature fields show little differences between the two versions. For day 10 and day 20, HY and NH have virtually identical results. For day 30, however, slight difference in both the alongshore velocity and temperature fields can be noted. Further investigation revealed that the source is the differences on the horizontal plane, where the NH version features more meandering in the velocity and temperature fields (Fig. 7). This result is consistent with the findings of Chao and Shaw (2002) that downward convection caused by unstable stratification in a nonhydrostatic model would hasten the growth of upwelling meanders and filaments.

For WD-W4 setup, no apparent difference in the alongshore-averaged field can be noted between the HY and NH versions. Similar to the NR case, however, the difference in the patterns of alongshore variability is also present in the WD case, but statistically HY and NH results are almost identical, and no notable differences in meandering features are found between them.

To further investigate the nonhydrostatic effect quantitatively, an index called the Non-Hydrostatic Factor ($NHF$) is used (Tseng et al., 2005):
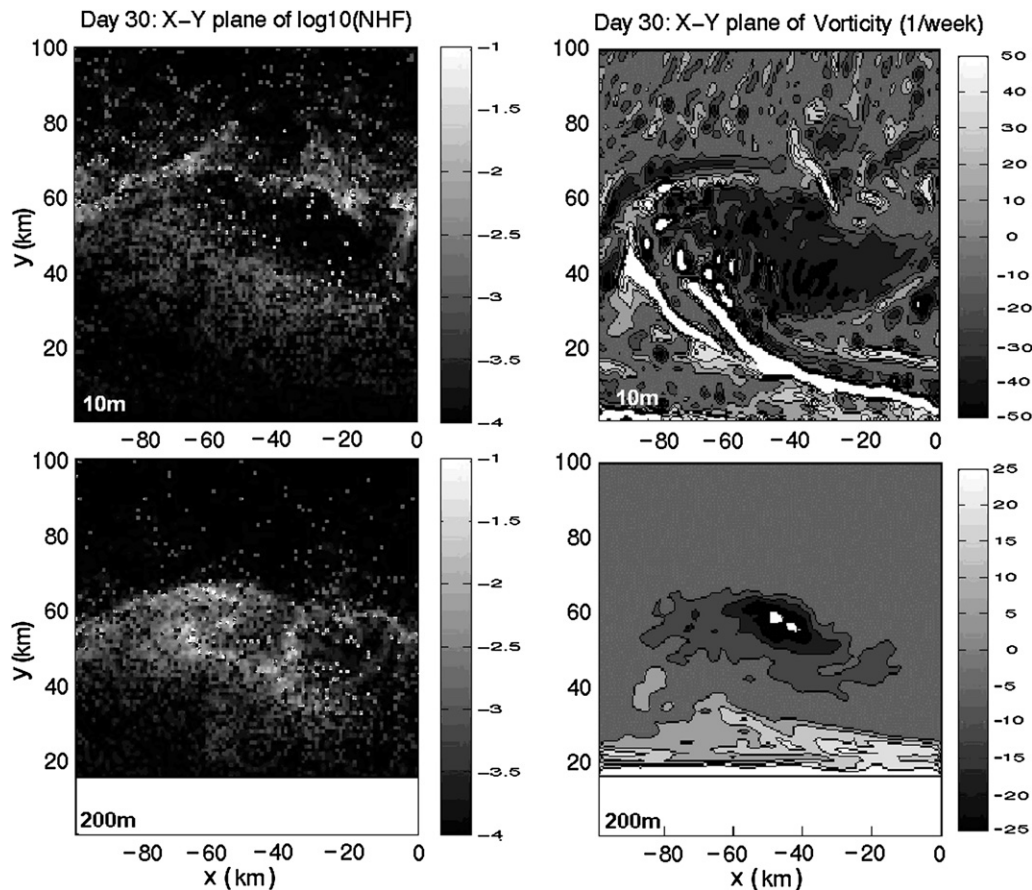


**Fig. 8.** The logarithm of $NHF$ on day 30 at 10 m (top left) and 200m (bottom left) with respective relative velocity fields (top right and bottom right) for comparison.

$$NHF = \left| \frac{\frac{\partial w}{\partial t} + u\frac{\partial w}{\partial x} + v\frac{\partial w}{\partial y} + w\frac{\partial w}{\partial z}}{\rho' g} \right|$$

where the density fluctuation is $\rho'(x,y,z) = \rho(x,y,z) - \rho_0(z)$, and $\rho_0(z)$ is the mean value of density $\rho$ at a constant depth $z$; and $u, v, w$ are the velocity components in $x, y, z$ directions, respectively. *NHF* estimates the relative significance of the nonhydrostatic term (vertical acceleration plus vertical advection) with respect to the reduced gravity term. Fig. 7 shows the logarithm of *NHF* on day 30 at different depths from the model runs using NR and W3. The *NHF*s are generally very small ($<O(10^{-3})$), but at some locations, particularly near the boundary of eddies, especially where sharp density (temperature) gradients exist, they are much larger ($>O(10^{-2})$). This is because nonhydrostatic effects are more pronounced when the horizontal length-scale of the process is small so that it is more comparable to vertical length-scale. From the time sequence of vertical sections of the alongshore-averaged *NHF*s (Fig. 8), the *NHF*s do not develop gradually, but are already significant at the beginning of the simulation. Also, the locations of large *NHF*s do not change rapidly over time and are limited to depths above 400 m, presumably due to the lack of stratification below 400 m.

## 4. Discussion of model results

### 4.1. Instabilities

In NR cases, the small features that first appeared near the coast are separated by 4–5 km, which agreed with a model study by Durski and Allen (2005). They concluded that these small features are baroclinic instabilities associated with the coastal upwelling front, and found that small features, which first appeared along the front, had an 8 km scale. They also found that if using fourth-order advection scheme instead of a third-order scheme in their model, the scale would have been 5 km. The 4–5 km scale instabilities present in our model is consistent with their results, since our model uses a fourth-order advection scheme. However, because their model employed a third-order advection scheme which had dissipative truncation error, and a smaller wind stress (0.3 dyn/cm$^2$) is used in their model forcing, they add artificial perturbations to the wind stress to generate instabilities. In our study, the instabilities appears due to the dispersive nature of the truncation error from the fourth-order advection scheme employed by the model. For advection schemes, even-order ones have dispersive truncation error and tend to generate small wiggles, while odd-order ones have dissipative truncation error and tend to dampen small wiggles (Sanderson and Brassington, 2002). We performed an NR test case simulation using background viscosities that are an order of magnitude larger than our initial value, under the strongest wind stress W4. We found no instabilities visible at the end of the 40-day simulation, and both the temperature and the currents were alongshore-invariant. This is because the high viscosity suppresses the wiggle-generating effect of the fourth order advection scheme.

To further confirm the baroclinic nature of the instability generated, we performed an eddy heat flux analysis by calculating the alongshore-averaged v′T′ and w′T′, where u′, w′ and T′ are deviations of cross-shore velocity, vertical velocity and temperature from their respective alongshore-averages (Dietrich, 1973). Fig. 9 shows the results on Day 10, 20, and 30. Alongshore-averaged temperature field was also overlaid for comparison. Near the surface v′T′ is negative and w′T′ is positive. The negative v′T′
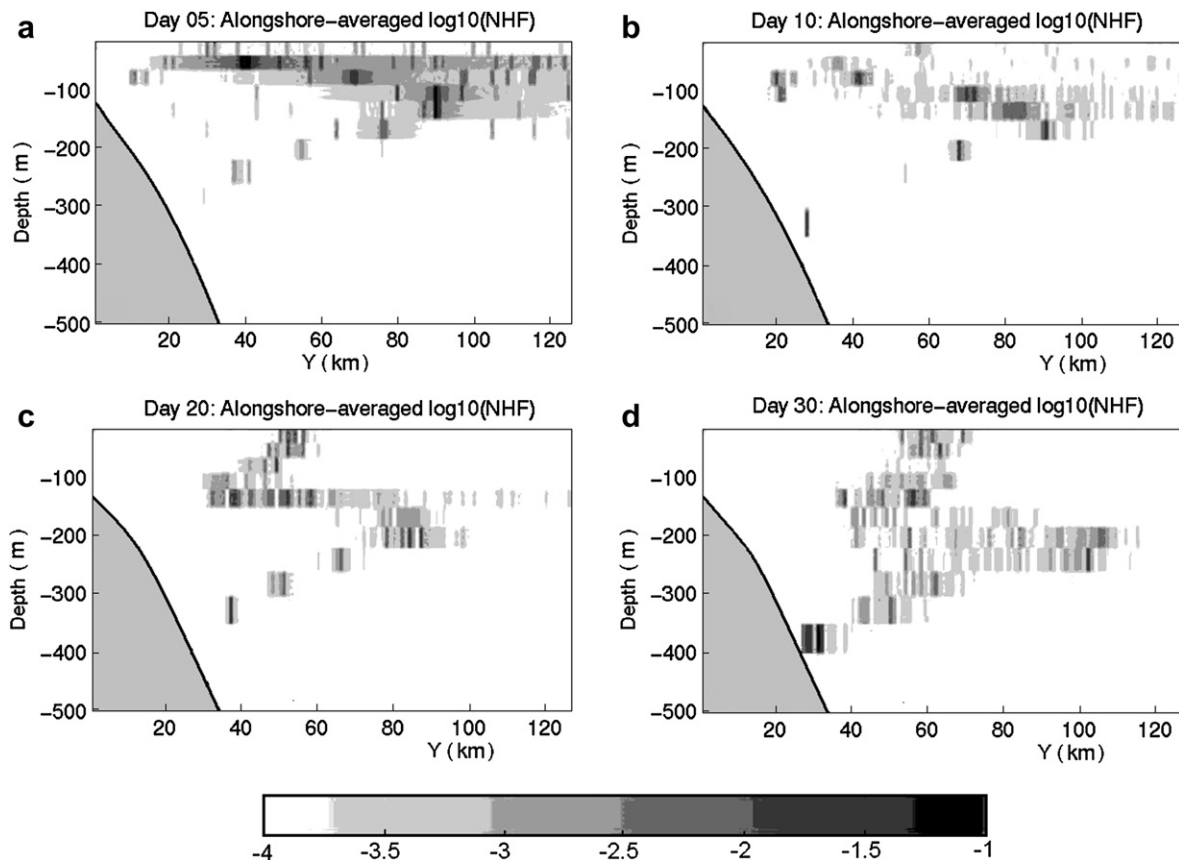


Fig. 9. The logarithm of alongshore averaged *NHF* on day 05,10, 20, and 30.

indicates conversion from mean available potential energy to eddy available potential energy, while the positive $\overline{w'T'}$ indicates conversion from eddy available potential energy to eddy kinetic energy. It is also noted that the conversion of the energy concentrated in the frontal region where cross-shore density gradient is most pronounced.

### 4.2. Frontal migration in NR cases

Information on upwelling frontal migration in real ocean is rather limited. Breaker and Mooers (1986) have used satellite imagery to estimate the offshore movement of the upwelling front off Pt. Sur, and found offshore velocities of about 0.5 km/day. They also found a high correlation coefficient between time-integrated wind stress and the upwelling area (about 0.9), which, however, they considered as possibly fortuitous. They believed the velocity they found to be more consistent with a Rossby wave dispersion theory (Philander and Yoon, 1982). Probably because the real wind changes direction and magnitude continuously, they did not further investigate the relationship between wind stress and upwelling frontal migration.

In our simulation, we got a linear dependence of the surface front migration speed on the wind stress: $u_f \sim 3\tau$, where $u_f$ is the frontal migration speed in cm/s and $\tau$ the surface wind stress in dyn/cm$^2$. This linear relationship is consistent with Ekman theory, in which the surface volume transport is given by $U_E = \tau/\rho f$. In our model, the surface transport is generally confined within the first $z$ level with a thickness of 20 m. Since $U_E = u_E \cdot d = \tau/\rho f$, then $u_E = \tau/\rho f d$, where if $\rho = 1$ g/cm$^3$, $f = 1 \times 10^{-4}$ and $d = 2 \times 10^3$ cm, then $u_E \sim 5\tau$. Thus, the offshore migration of the upwelling front is roughly 2/3 of surface Ekman transport speed. The even slower migration rate during the first phase when the front is close to shore might be explained by the decreased Ekman transport within the distance of the baroclinic Rossby radius, which is about 10 km in our case. The Ekman transport is 0 at the coast and $\tau/\rho f$ offshore, and the transition is believed to occur within the length scale of baroclinic Rossby radius offshore, where upwelling occurs (Brink, 1983; Lentz, 1995, 2001).

Fig. 10 shows the surface offshore speed (alongshore mean in solid bracketed by 3 standard deviations in dashed) plotted against offshore distance, compared with the theoretical Ekman transport speed (dash-dotted) calculated from the wind stress. Frontal location is also shown by a vertical line. It confirms that the surface velocity agrees well with the expected Ekman transport offshore of the front. Inshore of the front the instabilities seem to modify the offshore velocity to deviate from Ekman theory as shown in the Fig. 9. The front can be viewed as the boundary between turbulent flow and laminar flow. The reason for the front to move more slowly than the speed based on Ekman transport might be due to the transfer of energy from mean kinetic energy to turbulent kinetic energy at the front by mixing. However, other possibilities exist. We note that the '2/3' surface Ekman transport speed,
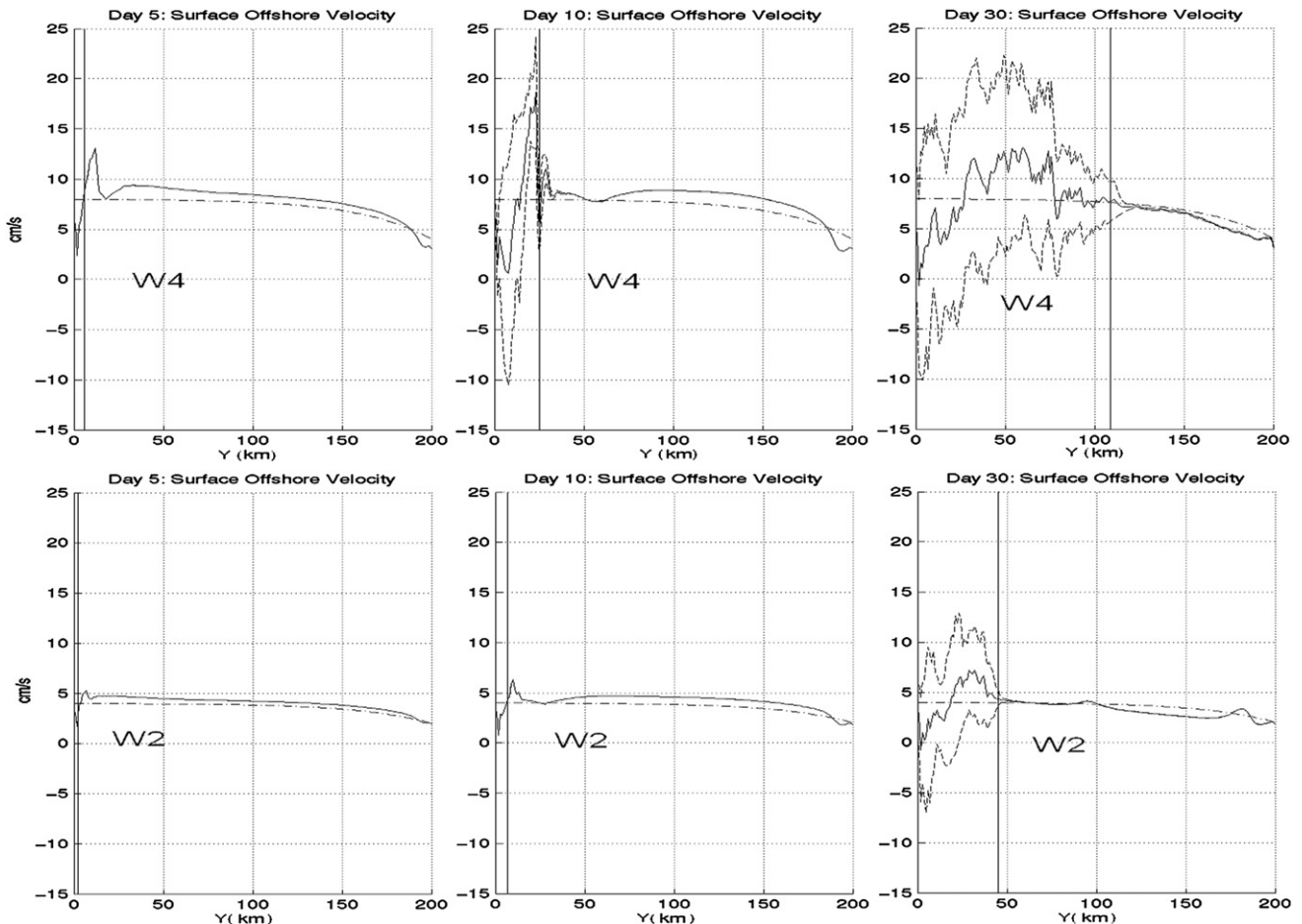


Fig. 10. Surface offshore velocity under W4 (upper) and W2 (lower). From left to right: day 05, day 10, and day 30.

however, agrees well with Breaker and Mooers (1986), who found by using a regression analysis, that the upwelling front moved more slowly than a material surface (about 2/3 Ekman transport), and gave a possible explanation of strong mixing and entrainment that took place across the front.

### 4.3. Discussion of WD cases

Unlike the narrow shelf case, there is no obvious migration of an upwelling front for the wide shelf case. Fronts with strong mixing developed at discrete phases. For the strongest winds, during the first five days, the upwelling front migrated in a manner similar to the narrow shelf case. Although figures are not shown, we find that by day 5, an upwelling front appeared at about 17 km offshore and mixing occurred inshore of the front. By day 8, a new front appeared at 45 km offshore, with intense mixing between the two frontal locations. By day 13, another front appeared at 58 km offshore with similar results. However, by day 16, the front weakens and starts to disappear. Mixing dominated the entire shelf out to 60 km offshore by day 20, and from that point on, no significant changes is observed.

The sudden appearance of these fronts seems to be related to our choice of vertical levels in the model and so is due to the topography and not the physics. However, we can conclude that there is no steadily migrating upwelling front, where the mixing is relatively stronger than ambient water. For the NR shelf topography, the lower gradient Richardson numbers reflect mixing due to overturning of denser upwelled, while for WD the gradient Richardson numbers reflect turbulent mixing due to bottom friction over a much shallower shelf. Therefore, mixing is stronger near the upwelling front (Fig. 4a) in NR, but more evenly distributed (Fig. 4b) in WD.

### 4.4. Assessment of nonhydrostatic effects

The comparison between the hydrostatic and nonhydrostatic versions of the model shows very little nonhydrostatic effect in our results, probably due to the idealized bottom topography setting. The region with relatively pronounced nonhydrostatic effects is near the boundary of eddies, and the NHF can be as large as 0.1. However, for the realistic topography used by Tseng et al. (2005), the NHF is found to be much larger near topographically irregularities.

### 5. Conclusion

Using an idealized numerical model, we simulated coastal upwelling for different wind stresses and different bottom topographies. We also compared hydrostatic and nonhydrostatic versions of the model. For narrow shelf, we find that the position of the major upwelling front is dependent on wind strength and duration. The offshore distance of the upwelling front is linearly dependent on wind duration, and the migration speed of the front is linearly dependent on wind stress, consistent with surface Ekman transport.

For wide shelf, no distinct migrating upwelling front is observed. There are also no eddies generated even after strong winds are imposed, because the inner shelf is flat and shallow. The wide, shallow shelves are also found to reduce isopycnal uplift and Ekman transport, and serve as a barrier to prevent the cold slope water from reaching the inner shelf.

Comparisons between hydrostatic and nonhydrostatic versions of the model show very similar results in alongshore-averaged fields. However, the accumulative effect of NH to enhance the growth of surface meandering can still be noticeable if the model

integration time is long enough ($\sim$30 days). The Non-Hydrostatic Factor (NHF) shows that while the nonhydrostatic effect is negligible in most area, it can be more pronounced near the boundary, especially at the steep front of an eddy.

### References

Allen, J., Walstad, L., Newberger, P., 1991. Dynamics of the coastal transaction zone jet 2. Nonlinear finite amplitude behavior. Journal of Geophysical Research 96 (C8), 14995–15016.

Beckmann, A., Haidvogel, D.B., 1993. Numerical simulation of flow around a tall seamount, part I: problem formulation and model accuracy. Journal of Physical Oceanography 23, 1736–1753.

Bernstein, R.L., Breaker, L., Whritner, R., 1977. California current eddy formation. Science 195, 353–359.

Bleck, R., 2002. An oceanic general circulation model framed in hybrid isopycnic-cartesian coordinates. Ocean Modelling 4, 55–88.

Breaker, L.C., Mooers, C.N.K., 1986. Oceanic variability off the central California coast. Progress of Oceanography 17, 61–135.

Brink, K.H., 1983. The response of stratified, frictional flow of shelf and slope waters to fluctuating large-scale, low-frequency wind forcing. Journal of Physical Oceanography 13, 103–116.

Casulli, V., Stelling, G.S., 1998. Numerical simulation of 3D quasi-hydrostatic, free-surface flows. Journal of Hydraulic Engineering-ASCE 124 (7), 678–686.

Chao, S.-Y., Shaw, P.-T., 2002. Nonhydrostatic aspects of coastal upwelling meanders and filaments off eastern ocean boundaries. Tellus 54A, 63–75.

Chen, C., Liu, H., Beardsley, R.C., 2003. An unstructured, finite volume, three-dimensional, primitive equation ocean model: application to coastal ocean and estuaries. Journal of Atmospheric and Oceanic Technology 20, 159–186.

Clarke, A.J., Brink, K.H., 1985. The response of stratified, frictional flow of shelf and slope waters to fluctuating large-scale, low-frequency wind forcing. Journal of Physical Oceanography 15, 439–453.

Clemente-Colon, P., Yan, X.-H., 1999. Observations of east coast upwelling conditions in synthetic aperture radar imagery. IEEE Transactions on Geoscience and Remote Sensing 37 (5), 2239–2248.

Danilov, S., Kivman, G., Schroter, J., 2005. Evaluation of an eddy-permitting finite-element ocean model in the North Atlantic. Ocean Modelling 10 (1–2), 35–49.

Dietrich, D.E., 1973. A numerical study of rotating annulus flows using a modified Galerkin method. Pure and Applied Geophysics 109, 1826–1861.

Dietrich, D.E., 1997. Application of a modified Arakawa "A" grid ocean model having reduced numerical dispersion to the Gulf of Mexico circulation. Dynamics of Atmospheres and Oceans 27, 201–217.

Dietrich, D.E., Haney, R.L., Fernandez, V., Josey, S.A., Tintore, J., 2004. Air-sea fluxes based on observed annual cycle surface climatology and ocean model internal dynamics: a non-damping zero-phase-lag approach applied to the Mediterranean Sea. Journal of Marine Systems 52 (1–4), 145–165.

Durski, S.M., Allen, J.S., 2005. Finite-amplitude evolution of instabilities associated with the coastal upwelling front. Journal of Physical Oceanography 35, 1606–1629.

Garvine, R.W., 2004. The vertical structure and subtidal dynamics of the inner shelf off New Jersey. Journal of Marine Research 62, 337–371.

Glenn, S.M., Crowley, M.F., Haidvogel, D.B., Song, Y.T., 1996. Underwater observatory captures coastal upwelling events off New Jersey. EOS Transactions AGU 77 (25), 233–236.

Haidvogel, D.B., Beckmann, A., 1998. Numerical models of the coastal ocean. In: Brink, K.H., Robinson, A.R. (Eds.), The Sea, vol. 10, pp. 457–482.

Halliwell, G.R., Pittock, H.L., Halliwell, V.M., Allen, J.S., 1986. The CODE Large-scale Meteorological, Sea Surface Temperature and Coastal Sea Level Data Set, 1980–1984.

Ham, D.A., Pietrzak, J., Stelling, G.S., 2005. A scalable unstructured grid 3-dimensional finite volume model for the shallow water equations. Ocean Modelling 10, 153–169.

Haney, R.L., 1991. On the pressure gradient force over steep topography in sigma coordinate ocean models. Journal of Physical Oceanography 21 (4), 610–619.

Haney, R.L., Hale, R.A., Dietrich, D.E., 2001. Offshore propagation of eddy kinetic energy in the California current. Journal of Geophysical Research 106, 11709–11717. doi:10.1029/2000JC000433.

Huyer, A., Smith, R.L., Paluszkiewicz, T., 1987. Coastal upwelling off Peru during normal and El-Nino times, 1981–1984. Journal of Geophysical Research – Oceans 92 (C13), 14297–14307.

Ikeda, M., Emery, W.J., 1984. Satellite-observations and modeling of meanders in the California current system off Oregon and northern California. Journal of Physical Oceanography 14 (9), 1434–1450.

Knowles, C.E., Singer, J.J., 1977. Exchange through a barrier inlet: additional evidence of upwelling off the northeast coast of North Carolina. Journal of Physical Oceanography 7 (1), 146–152.

Large, W.G., McWilliams, J.C., Doney, S.C., 1994. Oceanic vertical mixing: a review and a model with a nonlocal boundary layer parameterization. Reviews of Geophysics 32, 363–403.

Legrand, S., Deleersnijder, E., Hanert, E., Legat, V., Wolanski, E., 2006. High-resolution, unstructured meshes for hydrodynamic models of the Great Barrier Reef, Australia. Estuarine, Coastal and Shelf Science 68, 36–46.

Lentz, S.J., 1995. Sensitivity of the inner-shelf circulation to the form of the eddy viscosity profile. Journal of Physical Oceanography 25, 19–28.

Lentz, S.J., 2001. The influence of stratification on the wind-driven cross-shelf circulation over the North Carolina Shelf. Journal of Physical Oceanography 31, 2749–2760.

Lentz, S.J., Trowbridge, J.H., 1991. The bottom boundary-layer over the Northern California shelf. Journal of Physical Oceanography 21 (8), 1186–1201.

McClain, C.R., Pietrafesa, L.J., Yoder, J.A., 1984. Observations of gulf-stream induced and wind-driven upwelling in the Georgia Bight using ocean color and infrared imagery. Journal of Geophysical Research – Oceans 89 (NC3), 3705–3723.

McWilliams, J.C., 1996. Modeling the oceanic general circulation. Annual Reviews of Fluid Mechanics 28, 215–248.

Mellor, G.L., Ezer, T., Oey, L.Y., 1994. The pressure gradient conundrum of sigma coordinate ocean models. Journal of Atmospheric and Oceanic Technology 11, 1126–1134.

Mellor, G.L., Ezer, T., Oey, L.Y., 1998. Sigma coordinate pressure gradient errors and the seamount problem. Journal of Atmospheric and Oceanic Technology 15, 1122–1131.

Mellor, G.L., Yamada, T., 1982. Development of a turbulence closure model for geophysical fluid problems. Reviews of Geophysics and Space Physics 20, 851–875.

Mooers, C.N.K., Robinson, A.R., 1984. Turbulent jets and eddies in the California current and inferred cross-shore transports. Science 223 (4631), 51–53.

Narimousa, S., Maxworthy, T., 1985. Two-layer model of shear-driven coastal upwelling in the presence of bottom topography. Journal of Fluid Mechanics 159 (Oct), 503–531.

Narimousa, S., Maxworthy, T., 1987a. Coastal upwelling on a sloping bottom – the formation of plumes, jets and pinched-off cyclones. Journal of Fluid Mechanics 176, 169–190.

Narimousa, S., Maxworthy, T., 1987b. On the effects of coastline perturbations on coastal currents and fronts. Journal of Physical Oceanography 17 (8), 1296–1303.

Narimousa, S., Maxworthy, T., 1989. Application of a laboratory model to the interpretation of satellite and field observations of coastal upwelling. Dynamics of Atmospheres and Oceans 13 (1–2), 1–46.

Nelson, C.S., 1977. Wind Stress Curl over the California Current, NOAA Technical Report NMFS SSRF-714, 87pp., [NTIS PB-272310].

O'Brien, J.J., 1967. The non-linear response of a two-layer, baroclinic ocean to a stationary, axially-symmetric hurricane: part II. Upwelling and mixing induced by momentum transfer. Journal of Atmospheric Science 24, 208–215.

O'Brien, J.J., Hurlburt, H.E., 1972. A numerical model of coastal upwelling. Journal of Physical Oceanography 2, 14–26.

Pacanowski, R.C., Philander, S.G.H., 1981. Parameterization of vertical mixing in numerical models of tropical oceans. Journal of Physical Oceanography 11, 1443–1451.

Pain, C.C., Piggott, M.D., Goddard, A.J.H., Fang, F., Gorman, G.J., Marshall, D.P., Eaton, M.D., Power, P.W., de Oliveira, C.R.E., 2005. Three-dimensional unstructured mesh ocean modelling. Ocean Modelling 10 (1–2), 5–33.

Philander, S.G.H., Yoon, J.-H., 1982. Eastern boundary currents and coastal upwelling. Journal of Physical Oceanography 12 (8), 862–879.

Pitts, P.A., Smith, N.P., 1997. An investigation of summer upwelling across central Florida's Atlantic Coast: the case for wind stress forcing. Journal of Coastal Research 13 (1), 105–110.

Rosenfeld, L.K., Schwing, F.B., Garfield, N., Tracy, D.E., 1994. Bifurcated flow from an upwelling center – a cold-water source for Monterey Bay. Continental Shelf Research 14 (9), 931–964.

Sanderson, B., Brassington, G., 2002. Fourth- and fifth-order finite-difference methods applied to a control-volume ocean model. Journal of Atmospheric and Oceanic Technology 19, 1424–1441.

Semtner, A.J., 1995. Modeling ocean circulation. Science 269 (5229), 1379–1385.

Smith, R.L., 1968. Upwelling, Oceanographic and Marine Biology, An Annual Review, vol. 6. Allen, and Unwin, London. pp.11–46.

Song, Y.T., Haidvogel, D.B., Glenn, S.M., 2001. Effects of topographic variability on the formation of upwelling centers off New Jersey: a theoretical model. Journal of Geophysical Research 106 (C5), 9223–9240.

Swenson, M.S., Niiler, P.P., Brink, K.H., Abbott, M.R., 1992. Drifter observations of a cold filament off point Arena, California, in July 1988. Journal of Geophysical Research 97, 3593–3610.

Taylor, C., Stewart, H., 1959. Some upwelling along the east coast of Florida. Journal of Geophysical Research 64 (1), 33–40.

Trowbridge, J.H., Lentz, S.J., 1991. Asymmetric behavior of an oceanic boundary layer above a sloping bottom. Journal of Physical Oceanography 21, 1171–1185.

Tseng, Y.H., Dietrich, D.E., 2004. Guide for the DieCAST Ocean Model. http://efdl.as.ntu.edu.tw/research/diecast/download.html.

Tseng, Y.H., Dietrich, D.E., Ferziger, J.H., 2005. Regional circulation of the Monterey Bay region – hydrostatic versus nonhydrostatic modeling. Journal of Geophysical Research – Oceans 110, C09015. doi:10.1029/2003JC002153.

Tseng, Y.H., Dietrich, D.E., 2006. Entrainment and transport in idealized three-dimensional density current simulation. Journal of Atmospheric and Oceanic Technology 23, 1249–1269.

Tseng, Y.H., Ferziger, J.H., 2001. Effects of coastal geometry and the formation of cyclonic/anti-cyclonic eddies on turbulent mixing in upwelling simulation. Journal of Turbulence 2 (1), 014.

Wells, H.W., Gray, I.E., 1960. Summer upwelling off the northeast coast of North Carolina. Limnology and Oceanography 5 (1), 108–109.

White, L., Deleersnijder, E., 2007. Diagnoses of vertical transport in a three-dimensional finite element model of the tidal circulation around an island. Estuarine, Coastal and Shelf Science 74, 655–669.

Wooster, W.S., 1981. An upwelling mythology. In: Richards, Francis A. (Ed.), Coastal Upwelling. AGU, pp. 1–3.

Yankovsky, A.E., Garvine, R.W., 1998. Subinertial dynamics on the inner New Jersey shelf during the upwelling season. Journal of Physical Oceanography 28 (12), 2444–2458.